

EVOLUTION OF THE AERODYNAMIC STABILITY OF AN OSCILLATING ANNULAR COMPRESSOR CASCADE WITH INLET REVERSE FLOW CONDITION VARIATIONS

V.A.Chenaux¹ - H.Schönenborn² - P.Ott³

¹Ecole Polytechnique Fédérale de Lausanne, Switzerland.

Current affiliation: DLR- German Aerospace Center,

Institute of Aeroelasticity, 37073 Göttingen, Germany. Email: virginie.chenaux@dlr.de

²MTU Aero Engines GmbH, München, Germany. Email: harald.schoenenborn@mtu.de

³Ecole Polytechnique Fédérale de Lausanne, Switzerland. Email: peter.ott@epfl.ch

ABSTRACT

While the advancement of computing hardware now enables accurate predictions of flutter and forced response at normal flow conditions during the compressor design phase, aeroelastic computations at off-design or reverse flow conditions remain a challenging task. During the flow reversal sequence of a surge cycle, complex aerodynamics occur which make the accurate prediction of the unsteady forces acting on the blades difficult to assess.

The main objective of this study is to increase the physical understanding of the unsteady contributions acting on the blades during the reverse flow sequence of a typical deep surge cycle. The approach adopted consisted in performing aeroelastic investigations on an annular compressor cascade at established reverse flow conditions. The cascade blades were equipped with unsteady pressure transducers and were excited to controlled oscillations in travelling wave mode. In this paper, the blade surface fluctuating pressures recorded are analyzed for different flow operating conditions. The measurements enable the determination of the blade aerodynamic stability as well as the identification and characterization of the unsteady physical mechanisms present during the surge blow-down phase.

NOMENCLATURE

c	Blade chord length
c_p	Steady - state pressure coefficient
c_{pu}	Unsteady pressure coefficient
EAV	Ensemble Average Technique
FFT	Fast Fourier Transform
IBPA, σ_k	Interblade phase angle
i	Blade number
j	Unsteady pressure transducer number
LE	Blade leading edge
L_i	Components of the influence coefficient matrix
M	Mach number
N	Total number of blades ($N = 20$)
p	Local pressure
\hat{p}	Amplitude of the i^{th} UPT first harmonic
x	Chordwise coordinate
PS	Blade pressure side
SS	Blade suction side
TE	Blade trailing edge
t	Time variable
Φ	Phase shift between blade and UPT signal
Ξ	Global aerodynamic damping coefficient

Ω	Angular frequency
$\alpha(t)$	Blade motion signal
$\hat{\alpha}$	Blade motion amplitude
β	Flow angle
δ	Angular vibration amplitude of the blade
1	Inlet flow conditions
2	Outlet flow conditions
tot	Total conditions
stat	Static conditions

INTRODUCTION

Figure 1 presents the four typical sequences of a deep surge event. The flow becomes unstable (point 0) and the surge cycle starts at point 1. The cause is due to a flow blockage, resulting in a shock wave which moves upstream to the engine inlet (an expansion wave moves downstream as well towards the combustor chamber, but is of less structural consequence). An axisymmetric flow reversal occurs, corresponding to a negative compressor characteristic. After this, the flow is reversed until the volumes associated with the compressor are empty. During this period (point 2), the engine depressurizes or "blow-down" as air continues to escape via the normal turbine route as well as the flow reverses through the compressor. As the blow-down progresses, the internal pressure levels drop until the pressure ratio across the compressor falls below the shut-off head. In the time scale of surge events, blow-down phase is a relatively long event, lasting approximately 40-50 milliseconds, depending of the size of the combustor section volume. Once the shut-off head is reached, the compressor resumes pumping (point 3) and repressurizes the system (point 4), typically requiring another 50 milliseconds to approach pre-surge pressure levels. A repeat of the initial surge event becomes possible, unless the condition which causes the initial engine surge is alleviated.

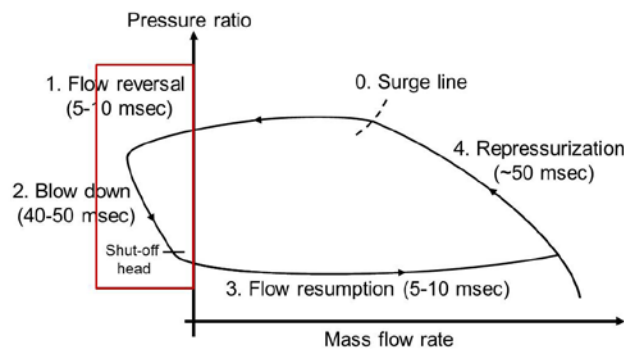


Figure 1. Typical sequences of a deep surge event.

From a structural point of view, if the entire surge cycle lasts 1/10 seconds, the phenomenon is severe: the forces induced by the surge shock wave endanger compressor blades, but also rotor shafts and inlet components. High pressure ratios induce sudden and dramatic depressurization, as well as sudden important loading changes, yielding high internal structure stress levels. Since these damaging consequences must be avoided imperatively, it is important, firstly to be able to predict the surge instability, and secondly, to understand the physical mechanisms and characteristics of the reverse flow phase of surge.

Literature off-design flow conditions

During the past decades, a considerable amount of investigations were carried out in order to understand and control surge phenomena. First studies were oriented towards surge aerodynamics and were based either on experimental data or simplified 2D numerical computations. Greitzer [1] and [2] proposed a non-linear single parameter model to assess the transient performance of a compressor to determine the occurrence of surge or rotating stall in low speed axial engines. Koff and Greitzer [5] characterized the 2D flow structures at reverse flow conditions and reported the

presence of a large separation region on the blade SS. A stagnation area on the blade PS was also documented.

Carstens et al. [8] performed numerical simulations associated to an annular turbine cascade operated at off-design flow conditions, for an impingement angle of 22° . They showed the difficulties of 2D Euler codes to capture the complex flow field characteristics associated to the blade SS stalled zone.

On typical HP compressors, surge duration corresponds to about hundred revolutions, which is sufficient to consider a steady-state flow field regulated by the compressor geometry and operating conditions. Di Mare et al. [16] performed 3D numerical simulations to characterize the "steady-state" reverse flow field in one compressor stage, representative of the quasi-steady conditions at peak flow reversal during surge. This investigation provides a focused comprehension of the aerodynamics associated to the surge blow-down phase.

Considering the aspect of blade loading, surge mechanisms are still not fully understood. Surge-induced loads were referenced by Mazzawy [3] with the development of a model estimating the blade loading in the entire compressor system. Gamache and Greitzer [6] carried out investigations focused on the surge blow-down phase, but the factors influencing blade loading levels were not highlighted. Thanks to the improvement of computational performance, complex models of compressor system surge progressively appear: Niazi [12] presented a methodology to simulate off-design steady-state flow conditions and Vahdati et al. [13] simulated a complete core compressor with application to aeroelasticity. Longley [15] developed a 3D blockage-mixing method able to calculate stall and surge transients to derive the compressor map at reverse flow condition. Conclusions put in evidence that the blade loading is essentially related to the initial pressure wave mechanism (hammershock pulse).

From an aeroelastic point of view, flutter and forced response analysis were widely investigated for standard flow conditions, with combined fluid/structure approaches (Marshall [9], Srinivasan [11]). Schöenborn [14] applied these procedures to surge flow operating conditions. For several mode shapes, Di Mare et al. [16] also performed flutter stability computations applied on a rotor subjected to reverse flow conditions. The resulting damping curve exhibits a sine shape, but the level of damping is reduced compared to normal flow conditions. Recently, Schöenborn et al. [19] identified that the large vibratory blade response is due to the pressure pulse (first mechanism) but also to a second mechanism prevailing during reverse flow conditions and acting on the blade loading level. A new flutter region was detected, engendered by aerodynamically unstable flow conditions.

Chenaux et al. [17] performed experimental investigations on an annular compressor cascade operated at different inlet reverse flow conditions. They characterized the influence of different reverse flow operating conditions on the steady-state flow field. Associated steady-state CFD computations were in very good agreement with the measured data and can be set as a basis for the aeroelastic computations. Controlled vibration measurements were then performed: for one interblade phase angle (IBPA), the unsteady pressures measured were compared to the associated numerical results (Schöenborn et al. [18]). CFD results revealed underpredicted pressure levels on the blade SS, inside the separation zone. This highlights the difficulty of linearized codes to capture the complex unsteady flow phenomena present at reverse flow conditions. The blade global stability was also computed, indicating possible instabilities for some operating points. Based on the aeroelastic measurement results for a reference operating point, Chenaux et al. [21] identified a strong blade-to-blade interaction mechanism present at reverse flow conditions. The aim of the present publication is to analyze and compare the experimental aeroelastic results, this time for different inlet flow angles and Mach numbers. Unsteady blade surface pressure measurement results are analyzed in order to identify and characterize other physical mechanisms present during the reverse flow phase of a deep surge cycle. The evolution of the blade aerodynamic stability with inlet reverse flow condition variations is highlighted. Associated upstream, downstream and casing wall steady-state flow fields are not included here but are detailed in Chenaux [20].

EXPERIMENTAL SETUP

The measurements were carried out at EPFL, in the Non-Rotating Annular Test Facility (**Figure 2**, detailed in Bölcs [4]). The annular compressor cascade consists of 20 blade suspension systems oscillating in their first torsional mode. The blade configuration was inverted with respect to normal compressor cascades, with blade trailing edge located at the inlet instead of outlet (**Figure 3**, left hand side). The inlet flow enters perpendicularly to the blade pressure side.

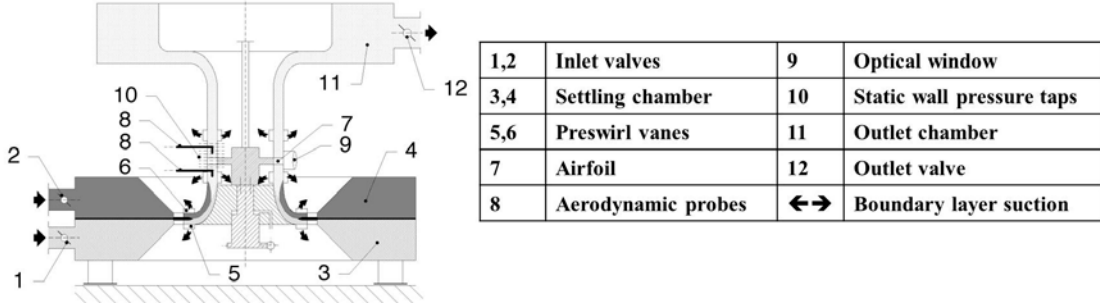


Figure 2. Schematic view of the Non-Rotating Annular Test Facility.

Each individual blade vibration system consists of a blade suspension element (spring), a mass element, a blade base and the blade itself (**Figure 3**, center). The spring design selected for the current investigation is cross-shaped to force controlled vibration measurements in the first torsional mode. Its shape and stiffness determines the final blade suspension system natural frequency. The natural frequency of the 20 individual blade suspension systems is included within a range of 283 and 298 Hz. The mass element is designed to maximize the moment of inertia around the torsional axis (corresponding to the blade center of gravity). Transformer plates are fixed on the mass element bottom side. To perform aeroelastic measurements, the twenty blade vibration systems are individually excited to oscillations in travelling wave mode using their associated electromagnetic exciter (**Figure 3**, right hand side, element number 8). The blade i motion is controlled with a displacement transducer in both its amplitude $\hat{\alpha}$ and IBPA σ_k , according to:

$$\alpha_i(t) = \hat{\alpha} \cdot \cos(\Omega t - i\sigma_k) \quad (1)$$

The signal monitoring is used as a feedback in the control loop. Cascade blades were equipped with steady-state and unsteady pressure taps (tapings connected to unsteady pressure transducers of type KULITE XCQ-062) to acquire the blade surface pressure distribution in one steady-state and two unsteady blade passages at 50% span. The pressure taps positions are detailed in **Figure 4**. The steady-state flow field characteristics were assessed using 5-hole aerodynamic probes, placed up- and downstream of the test section. The blade surface unsteady pressure distribution was recorded for each defined IBPA. For all unsteady pressure transducers (UPT) j , the first harmonic \hat{p}_j is extracted using a Fourier transform, and is related to the i^{th} blade pitching motion (Equation 2):

$$\hat{p}_j(t) = \hat{p}_j \cdot \cos(\Omega t - i\sigma_k + \Phi_j) \quad (2)$$

where Φ is the phase relationship between the unsteady pressure and the motion of the blade they are mounted on.

Table 1 presents the measurement matrix selected for the investigations. Test case 7102 stands at the crossroad of both variations (inlet flow angle and Mach number) and was selected as the reference case. Steady-state and unsteady experimental results for this test case are presented in reference [21]. Considering the parameters of variation, two different inlet Mach numbers (test case 7104 and 7105) and two different inlet flow angles (test case 4502, 5502) were tested. The associated experimental results are presented in this paper. The operating conditions selected correspond to the widest range achievable with the cascade configured for reverse flow conditions.

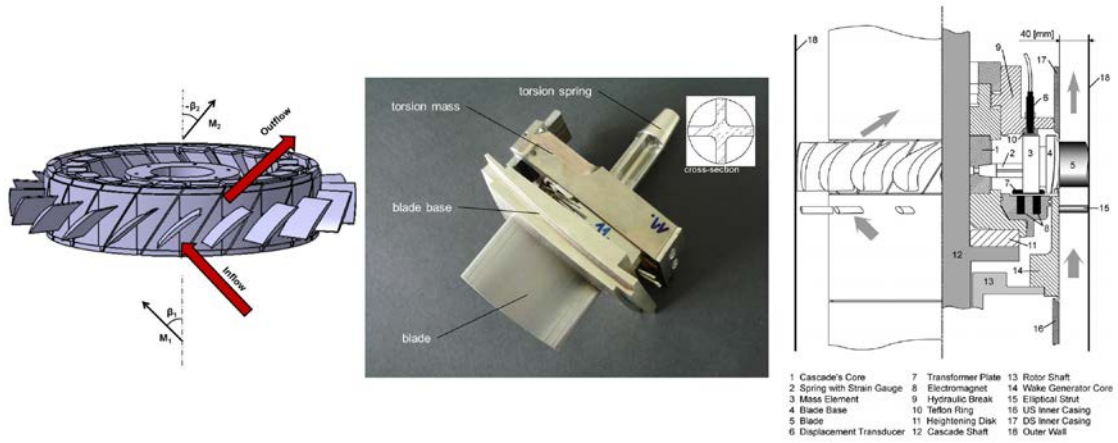


Figure 3. Left: cascade model and configuration dedicated to reversed flow investigations. Center: blade vibration mechanism. Right: cascade vibration system.

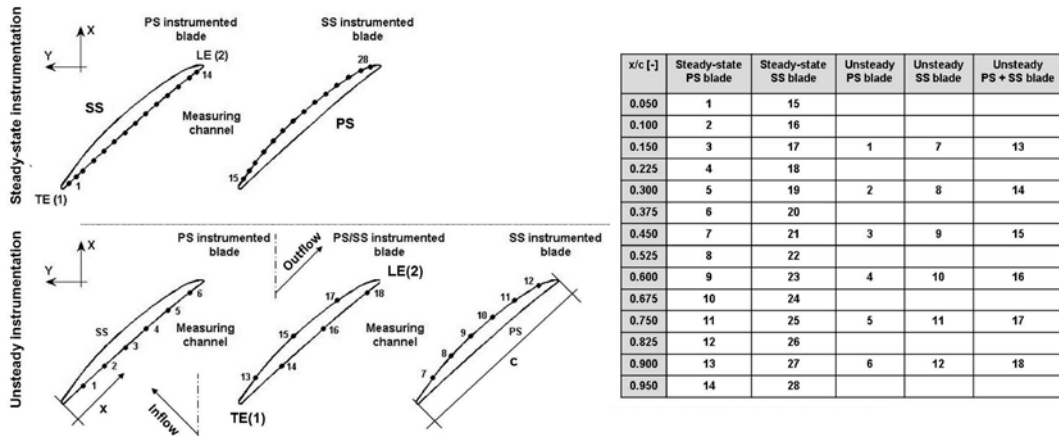


Figure 4. Upper left: blade surface steady-state and unsteady instrumentation. Bottom left: blade unsteady surface measurement positions. Right: table with measurement positions.

Inlet flow angle β [°] / Inlet Mach number M [-]	0.2	0.4	0.5
45	4502		
55	5502		
71	7102	7104	7105

Table 1. Left: measurement matrix. Right: 2D reverse flow blade setup

STEADY-STATE RESULTS

The steady-state blade surface pressures measured were converted to a pressure coefficient defined as (Equation 3):

$$c_p = \frac{P - p_{1,stat}}{p_{1,tot} - p_{1,stat}} \quad (3)$$

Figure 5 left and right presents the steady-state pressure coefficient measured for inlet Mach number and inlet flow angle variations respectively. For reference case 7102 ($\beta_1 = 71^\circ$ and $M_1 = 0.2$), on the blade PS, a static pressure corresponding to unity indicates the presence of a stagnation area localized between $x/c = 0.25$ and $x/c = 0.4$. This stagnation area is followed by a significant pressure drop (steep negative slope), indicating that the flow is accelerated towards the pressure side outlet (blade LE). On the blade SS, negative c_p values remain in the same order of magnitude along blade chord length. This trend illustrates the presence of a large separation area. The flow is

kept at the same velocity level up to $x/c = 0.78$, where a slight acceleration occurs, indicating a flow reattachment towards the blade SS LE.

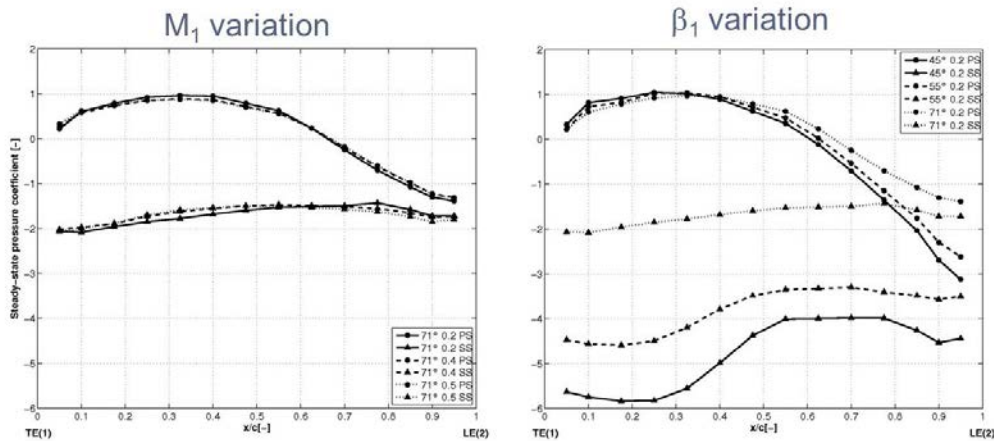


Figure 5. Steady-state blade surface pressure coefficient for inlet Mach number and inlet flow angle variations (left and right respectively).

Considering the steady-state pressure coefficient distribution analyzed for the reference case 7102, no significant evolution is noticed on the PS when increasing the inlet Mach number. However, the acceleration onset (and thus the reattachment) occurring at the aft SS moves upstream as the Mach number increases.

Increasing the inlet flow angle has a significant effect on the blade surface pressure distribution. On the blade pressure side for high inlet flow angles, the stagnation region moves downstream and is followed by a reduced acceleration up to blade PS LE. On blade SS, for test cases 4502 and 5502, the pressure levels off twice along the blade chord, whereas for test case 7102 one single, extended constant pressure coefficient area can be observed. Blade loading is higher for low inlet flow angles, inducing a larger acceleration of the flow through the blade channel. This is due to an increase of the axial velocity contribution, to the detriment of the circumferential velocity component.

UNSTEADY RESULTS

For test case 7102 and $IBPA = 180^\circ$, **Figure 6** presents the FFT results of two blade surface unsteady pressure signals. The signals were processed using an Ensemble Average Technique (reference [10]). On the graph, they were normalized using the highest peak harmonic. The tapings positions are located on the blade PS TE (left hand side) and on the blade SS recirculation area (right hand side). The FFTs features of the other time dependent pressure signals are similar to those presented here. These results highlight that the unsteady pressure signals recorded during blade vibrations in the travelling wave mode are not purely sinusoidal. At least five significant peaks can be observed on the transducer signals, occurring at multiples of the fundamental harmonic.

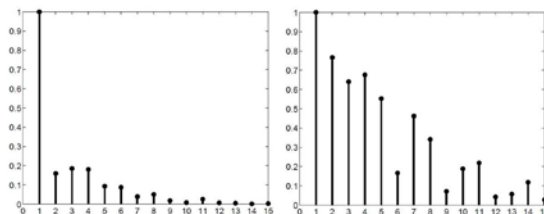


Figure 6. Normalized FFT results using the EAV technique, for one unsteady pressure signal located on the blade PS (left) and for one blade SS signal located in the stall zone area (right).

The fluctuating pressures measured on each UPT were converted to an unsteady pressure coefficient (Equation 4):

$$c_{pu} = \frac{|\hat{p}|}{\delta[\text{rad}] \cdot (p_{1,tot} - p_{1,stat})} \quad (4)$$

where \hat{p} is the amplitude of the signal fundamental harmonic in the frequency domain, and δ the angular vibration amplitude of the blade.

Figure 7 presents the evolution of the blade SS unsteady pressure coefficient amplitudes (top) and phase shift (bottom) with inlet flow angle variations (side by side arrangement of all IBPAs σ_k). For test case 7102, values measured corresponding to IBPA = 306° and 324° were not included, since the blade vibration signal analysis revealed non constant controlled vibration conditions. Both IBPAs were interpolated from the neighboring IBPAs results. Dark shades on the phase viewgraph represent negative phase values (unsteady pressure signal lags the blade motion signal) whereas light shades indicate a phase lead. The incertitude of the time-dependent pressure signals is estimated within the range of $\pm 17\%$ for the amplitude and $\pm 12\%$ for the phase. This incertitude is primarily due to the variations of the mainstream flow conditions, the cascade vibration mode as well as the massive flow disturbance effects occurring at reverse flow conditions. Note that a detailed description of systematic and random errors expected on the unsteady pressure signals is included in reference [20].

The SS unsteady pressure amplitudes are higher up to $x/c = 0.4$. Comparing results for different inlet flow angles, lower unsteady pressure amplitudes can be observed for high inlet flow angles. This variation is associated to the effects due to the evolution of the stall zone structure, combined with the blade loading effects. Steady-state results highlighted that the inlet flow angle variations had an influence on the recirculation zone in terms of energy and spatial extension. They also showed that this stall zone located on the blade suction side has an impact on the blade steady-state loading. For lower inlet flow angles, the zone is more energetic, thus generating higher pressure fluctuations.

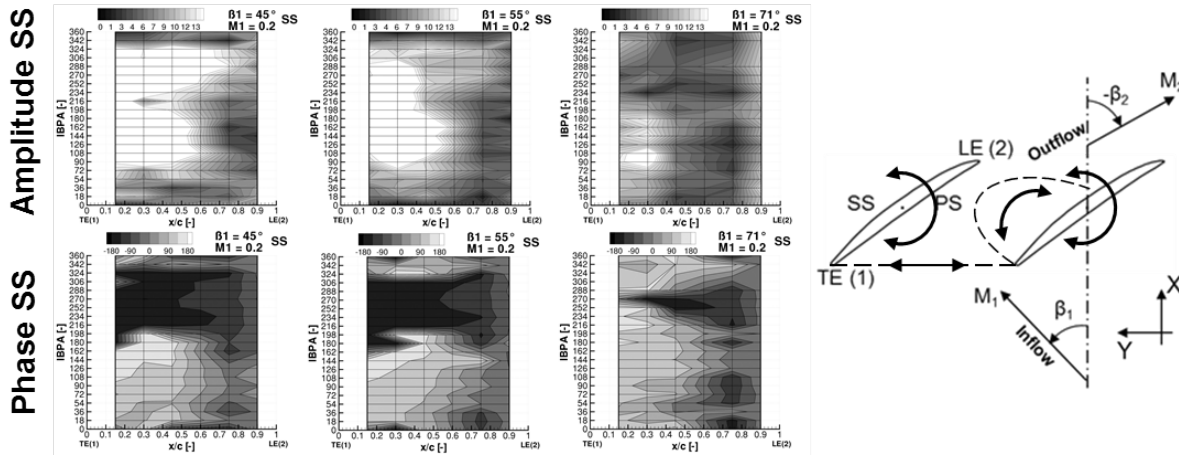


Figure 7. Evolution of the blade SS c_{pu} amplitude (top) and phase shift (bottom) with inlet flow angle variations (test cases 4502, 5502, 7102). Right: Scheme of the separation zone oscillation and passage throat area modification.

Phase shift results show a high dependency on the IBPA and on the blade chord position. For test case 7102, positive phases are identified from blade TE up to $x/c = 0.5$ for almost all IBPAs, whereas the phase shift is negative for almost all IBPAs from mid-chord up to blade leading edge. For IBPA = 270° the phase remains negative along the entire chord length. Associated computations indicate that for test case for 7102 ($M_1 = 0.2$ and $\beta_1 = 71^\circ$), this IBPA might be a source of acoustic resonance (phenomenon described in [10]). Stronger dependencies on the IBPAs can be identified for lower inlet flow angles. The phase lag present at the TE area for IBPA = 198° up to 360° decreases when increasing the inlet flow angle, while the phase lag observed in the LE area for IBPA = 0° to 180° increases when increasing the inlet flow angle. The physical phenomenon which prevails is most likely due to the configuration of the neighboring blades. This

is mainly due to the modification of the inlet passage throat area (**Figure 7**, right hand side), combined with the effect of the oscillation of the separation zone on the blade forward suction side (TE up to mid-chord). For an IBPA = 90°, the upstream section of the blade passage is enlarged. For an IBPA = 270°, the inlet passage is slightly closed. In case of oscillating blades, this overpressure is time dependent and is in phase with the blade excitation. This mechanism is expected to have an influence on the separation zone structure (which might act as a resistance) and amplifies the impact of the stall zone oscillations. The phenomenon is amplified when the mass flow is increased. Since test case 7102 has a lower axial velocity than the other test cases, the pressure signal phase dependency on the IBPA is decreased.

Figure 8 presents the normalized damping coefficient (definition (5) based on reference [20]) for test case 7102. Experimental results are represented with black markers for all IBPAs, except for IBPA = 306° and 324°. These IBPAs were removed since no proper controlled vibration condition was obtained. The black line represents the fitting curve based on Fourier series. The aerodynamic damping coefficient is normalized due to confidentiality reasons. Four harmonics are necessary to fit the 20 measurement results corresponding to each IBPA. The high number of harmonics required to fit the curve on the measurement points reveals that the blade global aerodynamic behavior for a cascade operated at reverse flow conditions cannot be determined using a simple sine curve. Within this frame, the neighboring blades provide a major contribution to the unsteady aerodynamic force distribution acting on the blade: the blade-to-blade aerodynamic interaction is expected to be extended in more than just one blade passage.

$$\Xi = -\text{Im}(\tilde{c}_M \cdot \tilde{z}) \quad (5)$$

The normalized global aerodynamic damping coefficient evolution with inlet flow angle variations is presented in **Figure 9**, left hand side. The curves correspond to the Fourier series fitting curves based on four harmonics (same approach as the one applied for test case 7102). Results show that four harmonics are necessary but sufficient to fit the curve on the discrete measurement results. This highlights that varying the inlet flow angle induces similar blade-to-blade interactions as for the reference case 7102. Based on the influence coefficient approach, **Figure 10** illustrates that the force experienced by the blade due to its own motion (corresponding to the real component L_0 on the viewgraph) decreases with increasing the inlet flow angle (corresponds to the average offset in reference [7]).

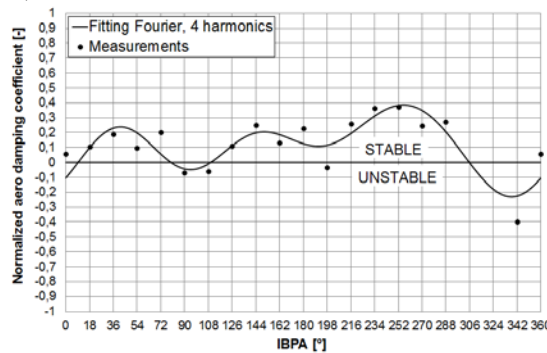


Figure 8. Normalized global aerodynamic damping coefficient for test case 7102 ($M_1 = 0.2$ and $\beta_1 = 71^\circ$), based on Fourier series with 4 harmonics (black curve), fitted on the measurement results at each IBPA (black markers).

Compared to reference case 7102, the range of the normalized global damping coefficient is higher for lower inlet flow angles. This is due to the contribution of the blade SS higher unsteady pressure amplitude levels. Negative aerodynamic damping values can be observed for IBPA = 18° to 144° for test case 4502 and for IBPA = 0° to 90° for test case 5502, yielding the conclusion that lower inlet flow angles might induce aerodynamic unstable conditions and increase flutter risks.

The normalized aerodynamic damping coefficient corresponding to the inlet Mach number variation is presented in **Figure 9**, right hand side. Again, four harmonics were included to fit the

measurement results. Increasing the inlet Mach number has a reduced influence on the range of the normalized global aerodynamic damping values. The global blade aerodynamic stability slightly increase with increasing the inlet Mach number: test cases 7104 and 7105 show positive or near zero damping coefficient values for all IBPAs, suggesting that flutter risks are reduced. This is might be caused to the aerodynamic losses, increasing with increasing the Mach number.

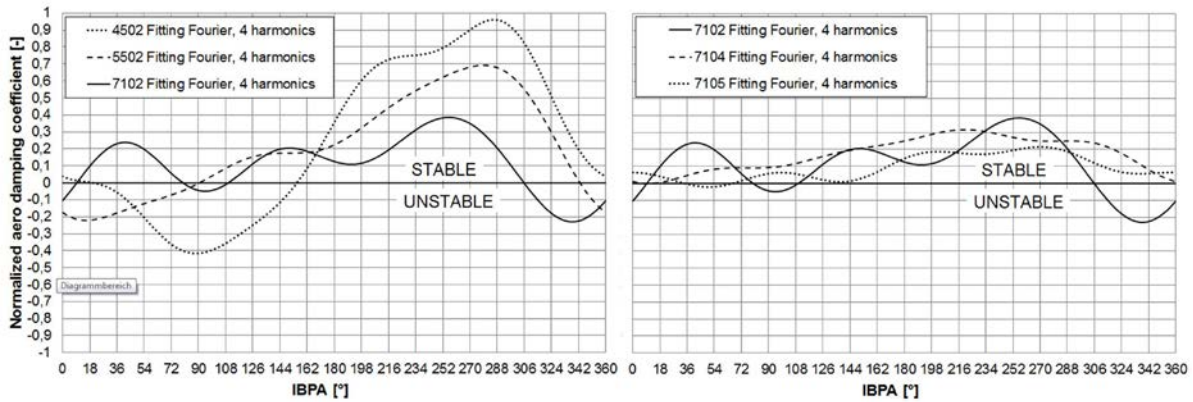


Figure 9. Evolution of the normalized global aerodynamic damping coefficient with variations of inlet flow angle (left) and inlet Mach number (right).

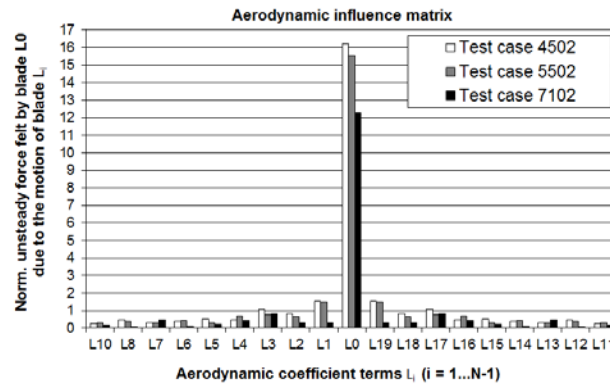


Figure 10. Evolution of the L_i ($i = 0, \dots, N-1$) real components of the influence coefficient matrix with inlet flow angle variations. Values represent the force felt by one blade (L_0 component) due to the motion of the neighboring blades (L_i components).

CONCLUSIONS

Steady-state and unsteady blade surface pressure distributions were measured on an annular compressor cascade subjected to controlled vibration at established reverse flow conditions. The aeroelastic measurements were performed for different inlet flow conditions; this enabled the identification and the characterization of two main physical mechanisms, which have an impact on the aerodynamic stability of the cascade:

- The blade-to-blade interactions mechanism.
- The oscillation of the blade SS recirculation zone.

In particular, increasing the inlet flow angle yields:

- A recirculation zone spatially extended but less energetic. This feature has a stabilizing effect on the blade aerodynamic behavior.
- A reduced impact of the inlet passage throat area variation depending on the IBPA imposed.

Based on the real component of the influence coefficient matrix, increasing the inlet flow angle reduces the blade unsteady loading.

ACKNOWLEDGEMENTS

The investigations are part of a project of the MTU Aero Engines GmbH, in the frame of a German research project, LuFo IV. The authors would like to acknowledge the financial support provided and the authorization for publishing the results here.

REFERENCES

- [1] Greitzer E. M., "Surge and Rotating Stall in Axial Flow Compressors, Part I: Theoretical Compression System Mode", ASME Journal of Engineering for Power, pp.190-217, 1978.
- [2] Greitzer E. M., "Surge and Rotating Stall in Axial Flow Compressors, Part II: Experimental results and comparison with theory", ASME Journal of Engineering for Power, pp.190-217, 1978.
- [3] Mazzawy, R.S., "Surge Induced Structural Loads in Gas Turbines", Transactions of the ASME, 162/ Vol. 102, 1980.
- [4] Bölcs A., "A Test Facility for the Investigation of Steady and Unsteady Transonic Flows in Annular Cascades", Proc. of ASME, 83-GT-34, 1983.
- [5] Koff S.G., Greitzer E.M., "Axisymmetrically stalled flow performance for multistage axial compressors", Journal of Turbomachinery, Vol. 108, Nr.2, 1986.
- [6] Gamache R. N., Greitzer E. M., "Reverse Flow in Multistage Axial Compressors", AIAA-paper 86-1747, AIAA/ASME/SAE/ASEE 22nd Joint Propulsion Conference, Huntsville, USA, 1986.
- [7] Platzer M.F., Carta F.O., "AGARD Manual on Aeroelasticity in Axial-Flow Turbomachines", Journal of Turbomachinery, Tome I and II, 1988.
- [8] Carstens V., Körbacher H., "Comparison of Experimental and Theoretical Results for Unsteady Transonic Cascade Flow at Design and Off-Design Conditions", Proc. of the ASME Turbo Expo 1993, Cincinnati, USA, 1993.
- [9] Marshall J.G., Imregun M., "A review of Aeroelasticity Methods with Emphasis on Turbomachinery Applications", Journal of Fluids and Structures, Vol.10, pp. 237-267, 1996.
- [10] Körbacher H., "Experimental Investigation of the Unsteady Flow in an Oscillating Annular Compressor Cascade", Ph.D. Thesis, Lausanne, Switzerland, 1996.
- [11] Srinivasan A.V., "Flutter and Resonant Vibration characteristics of Engine Blades", Journal of Engineering for Gas Turbines and Power, Vol.119, pp.742-775, 1997.
- [12] Niazi S., "Numerical Simulation of Rotating Stall and Surge Alleviation in Axial Compressors", Ph.D. Thesis, 2000.
- [13] Vahdati M., Simpson G., Imregun M., "Unsteady Flow and Aeroelastic Behaviour of Aero-Engine Core Compressors during Rotating Stall and Surge", Proc. of the ASME Turbo Expo 2006, Barcelona, Spain, 2006.
- [14] Schönenborn H., Breuer Th., "Aerodynamic and Mechanical Vibration Analysis of a Compressor Blisk at Surge", Proc. of ASME Turbo Expo 2004, GT2004-53579.
- [15] Longley J.P., "Calculating Stall and Surge Transients", Proc. of the ASME Turbo Expo 2007, Montreal, Canada, 2007.
- [16] Di Mare L., Krishnababu S. K., Mueck B., Imregun M., "Aerodynamics and Aeroelasticity of a HP Compressor during Surge and Reversed Flow", Proc. of ISUAAAT 12, London, UK, 2009.
- [17] Chenaux V., Schönenborn H., Ott P., "Experimental Investigations of the Aerodynamics of an Annular Compressor Cascade at Reversed Flow Conditions", ETC 2011, Istanbul, Turkey.
- [18] Schönenborn, H., Chenaux, V., Ott, P.: "Aeroelasticity at reversed flow conditions – Part 1: Numerical and Experimental Investigations of a Compressor Cascade with Controlled Vibration", ASME Paper GT2011-45034, Vancouver, Canada, 2011.
- [19] Schönenborn H., Breuer Th., "Aeroelasticity at Reversed Flow Conditions – Part 2: Application to Compressor Surge", ASME-Paper GT2011-45035, Vancouver, Canada, 2011.
- [20] Chenaux V.A., "Experimental Investigation of the Aeroelastic Stability of an Annular Compressor Cascade at Reverse Flow Conditions", Ph.D. Thesis, Lausanne, Switzerland, 2012.
- [21] Chenaux V.A., Schönenborn H., Ott P., "Experimental Investigation of an Annular Compressor Cascade at Reverse Flow Conditions", Proc. of ISUAAAT 13, Tokyo, Japan, 2012.